RSC Advances

PAPER

View Article Online
View Journal | View Issue

Cite this: *RSC Adv.*, 2018, **8**, 28

Effect of R-site element on crystalline phase and thermal stability of Fe substituted Mn mullite-type oxides: $R_2(Mn_{1-x}Fe_x)_4O_{10-\delta}$ (R = Y, Sm or Bi; x = 0, 0.5, 1)†

Sampreetha Thampy,‡[a] Nickolas Ashburn,‡[a] Thomas J. Martin,[b] Chenzhe Li,[c] Yongping Zheng,[a] Julia Y. Chan,[b] Kyeongjae Cho[a] and Julia W. P. Hsu*[a]

Combining experimental and theoretical studies, we investigate the role of R-site (R = Y, Sm, Bi) element on the phase formation and thermal stability of $R_2(Mn_{1-x}Fe_x)_4O_{10-\delta}$ (x = 0, 0.5, 1) mullite-type oxides. Our results show a distinct R-site dependent phase behavior for mullite-type oxides as Fe is substituted for Mn: 100% mullite-type phase was formed in (Y, Sm, Bi)$_2Mn_4O_{10}$; 55% and 18% of (Y, Sm)$_2Mn_2Fe_2O_{10-\delta}$ was found when R = Y and Sm, respectively, for equal Fe and Mn molar concentrations in the reactants, whereas Bi formed 54% O10- and 42% O9-mixed mullite-type phases. Furthermore, when the reactants contain 100% Fe, no mullite-type phase was formed for R = Y and Sm, but a sub-group transition to $Bi_2Fe_4O_9$ O9-phase was found for R = Bi. Thermogravimetric analysis and density functional theory (DFT) calculation results show a decreasing thermal stability in O10-type structure with increasing Fe incorporation; for example, the decomposition temperature is 1142 K for $Bi_2Mn_2Fe_2O_{10-\delta}$ *vs.* 1217 K for $Bi_2Mn_4O_{10}$. On the other hand, $Bi_2Fe_4O_9$ O9-type structure is found to be thermally stable up to 1227 K. These findings are explained by electronic structure calculations: (1) as Fe concentration increases, Jahn–Teller distortion results in mid band-gap empty states from unstable Fe^{4+} occupied octahedra, which is responsible for the decrease in O10 structure stability; (2) the directional sp orbital hybridization unique to Bi effectively stabilizes the mullite-type structure as Fe replaces Mn.

Received 31st August 2017
Accepted 7th December 2017

DOI: 10.1039/c7ra09699b

rsc.li/rsc-advances

1. Introduction

Functional materials based on transition metal oxides with mullite-type crystalline structure, $R_2M_4O_{10-\delta}$ (R = Y, rare-earth or Bi; M = transition metal), have gained much attention due to their interesting magnetic and multiferroic properties.[1,2] Recently, these compounds show great promise in energy applications, *e.g.* in solid oxide fuel cells,[3] as photocatalysts,[4] and NO_x oxidation catalysts,[5–7] and are considered as a potential alternative to platinum group metals. $R_2M_4O_{10-\delta}$ adopts the orthorhombic crystal structure of space group *Pbam* and consists of infinite chains of edge-sharing MO_6 octahedra along the *c*-direction (Fig. S1, ESI†). The structure can be classified according to two sub-groups depending on the oxygen concentration: $R_2Mn_4O_{10}$ (O10) and $R_2M_4O_9$ (O9). The two sub-groups differ in the MO_x (4h Wyckoff site) units that link the MO_6 (4f Wyckoff site) octahedral chains: edge-shared distorted MO_5 square pyramid in the O10-type (Fig. S1b, ESI†) or vertex-sharing MO_4 tetrahedra along the *ab*-direction in the O9-type (Fig. S1c, ESI†). The R atoms, which are in 3+ oxidation state, are located in the structural channels running parallel along the *c*-axis (Fig. S1a, ESI†).[8–12] It is clear that the transition metal (M) atoms, which occupy both the 4f- and 4h-Wyckoff sites, will strongly affect the structure formation and stability;[10,12] however, the role of R-site elements is less obvious.

Mn–Fe mullite-type oxides have been studied owing to their interesting magnetic behavior. As the ionic radii of Fe^{3+} and Mn^{3+} are similar, substituting Mn with Fe should not cause much lattice distortion.[12–19] However, because Fe^{4+} exhibits strong Jahn–Teller distortion and causes structure instability, sub-group transition from $R_2Mn_4O_{10}$ O10-type to $R_2Fe_4O_9$ O9-type is expected. Curiously, experimental studies reported such a sub-group transition in R = Bi Mn–Fe compounds,[12,19] but only the O10-type structure has been observed when R = Y

[a]*Department of Materials Science and Engineering, University of Texas at Dallas, Richardson, TX 75080, USA. E-mail: jwhsu@utdallas.edu*

[b]*Department of Chemistry and Biochemistry, University of Texas at Dallas, Richardson, TX 75080, USA*

[c]*School of Mechanical and Aerospace Engineering, Seoul National University, Seoul 151-742, Republic of Korea*

† Electronic supplementary information (ESI) available: Crystal structure of mullite-type oxides, *U* value table, Rietveld refinement plots, mullite phase purity table, experimental and simulated lattice parameters, density of states $Bi_2Fe_4O_{10}$ (O10) and $Bi_2Fe_4O_9$ (O9), density of states $Bi_2Mn_4O_9$ (O9) and $Bi_2Mn_4O_{10}$ (O10), TGA-DSC and XRD pattern of $Y_2Mn_2Fe_2O_{10-\delta}$. See DOI: 10.1039/c7ra09699b

‡ These authors contributed equally.

or rare earth elements.[13–18] In addition, except for Bi, no pure $R_2Mn_2Fe_2O_{10}$ mullite-type phase has been successfully synthesized with other R-site elements; impurity phases corresponding to perovskite or binary oxides or both are found in these compounds upon calcination at high temperatures and under high oxygen pressure.[13–17] Moreover, there are significant differences and conflicting reports on the maximum Fe concentration that supports the structure stability in Fe–Mn mullites.[12,19] Published literature reported the experimental observation, but lacked the fundamental understanding on the role of R-site elements on mullite-type phase formation and stability or why Bi compounds forms the stable mullite-type structure for all Mn–Fe compositions.

While R-site elements are trivalent, their electronic structure can differ significantly. Here, we carry out combined experimental and theoretical studies to understand the role of R-site elements on phase formation and thermal stability of $R_2(Mn_{1-x}Fe_x)_4O_{10-\delta}$ (R = Y, Sm, and Bi; x = 0, 0.5, 1) compounds. The three R-site elements are chosen because Y^{3+} has a closed shell, Sm^{3+} representing a lanthanide analogue with unpaired electrons, and Bi^{3+} with sp^3 hybridization. These compounds were synthesized by co-precipitation-calcination method. The crystalline phases were characterized using X-ray diffraction (XRD) and structure refinement was carried out by Rietveld method. The oxidation states of R, Mn, and Fe were determined by X-ray photoelectron spectroscopy (XPS). The thermal stability and phase transformation during decomposition was studied by thermogravimetric analysis (TGA) and differential scanning calorimetry (DSC). To explain the differences observed experimentally, we performed density functional theory (DFT) calculations with energy correction methodology previously employed to calculate the thermal stability of different $R_2Mn_4O_{10}$ compounds.[20] In addition, electronic structures were investigated to explain the R-site dependence as a function of Fe substitution. The insight gained through such combined experimental and theoretical studies will advance the design of mullite-type oxides with desired properties.

2. Experimental methods

2.1. Synthesis and characterization

$R_2Mn_4O_{10}$ (R : Mn = 1 : 2), $R_2Mn_2Fe_2O_{10-\delta}$ (R : Mn : Fe = 1 : 1 : 1), and $R_2Fe_4O_9$ (R : Fe = 1 : 2) were synthesized using analytical grade $R(NO_3)_3\cdot 6H_2O$, $Mn(CH_3CO_2)_2\cdot 4H_2O$, and $Fe(NO_3)_3\cdot 9H_2O$ precursors by co-precipitation method.[21] The precipitate obtained was then filtered and dried at 378 K overnight. The dried samples were ground and calcined at 773 K for 8 h in air to eliminate organic materials, followed by a second calcination step at high temperatures. For 100% Mn compounds, the calcination was carried out at 1373 K, 1273 K, and 1073 K for Y, Sm, and Bi, respectively, in air to obtain single-phase materials. For 50% Fe/50% Mn and 100% Fe samples, the calcination was carried out at 1073 K in air. This temperature was chosen to obtain mullite-type phase in all three R-site compounds. For Bi compounds, temperatures higher than 1073 K are too close to their decomposition temperatures; for Y or Sm compounds, the mullite-type phase cannot form below 1073 K. Thus, to get a meaningful comparison, synthesis conditions were kept constant.

X-ray diffraction data were collected two ways. First, the crystalline phases of the reaction products were characterized using powder Rigaku Ultima III X-ray diffractometer equipped with Ni-filtered Cu $K_{\alpha1,2}$ radiations ($\lambda_{K\alpha1}$ = 0.15406 nm, $\lambda_{K\alpha2}$ = 0.15444 nm).[22] The patterns were collected over a 2θ range from 20° to 60° with a step size of 0.02° and a scan speed of 0.2° per min. The measured diffraction patterns were compared to the powder diffraction files to identify the crystalline phases. To obtain accurate phase compositions and lattice parameters, X-ray powder diffraction data were also collected with a Bruker D8 Advance powder diffractometer operating at 40 kV/30 mA equipped with a LYNXEYE XE detector and a Cu Kα source ($\lambda_{K\alpha1}$ = 0.15406 nm, $\lambda_{K\alpha2}$ = 0.15444 nm) with a 0.06 mm incident beam and a 5.0 mm receiving slit with a Ni filter. Ground polycrystalline powders were placed on a low-background holder. X-ray diffraction data were collected over a 2θ range from 10° to 80° with a step size of 0.02° and an exposure time of 2 s rotating at five rotations per minute. The crystalline phases were first identified by comparing with reported crystal structure. Multi-phase Rietveld refinement was performed using DIFFRAC PLUS TOPAS 4.2 (Bruker AXS, Karlsruhe, Germany). For the Rietveld model, $\lambda_{K\alpha1}$ = 0.15406 nm wavelength was used.

X-ray photoelectron spectra were measured using a PHI5000 Versa Probe II (Physical Electronics Inc.) using a monochromatic Al Kα X-ray source (1486.6 eV). Peak fitting was performed using Multipak software as reported in our previous work.[21] The estimated error in binding energy measurements is ± 0.01 eV.

To measure the decomposition temperature, TGA and DSC measurements were carried out at a heating rate of 2 K min^{-1} from room temperature to 1273–1473 K in air (Q600, TA Instruments). To study the phase changes observed in the TGA-DSC measurements and to identify the crystalline phases of the decomposed products, we simulated the reactions by heating a different aliquot of the same sample in a muffle furnace (KSL-1100X, MTI Corporation) to obtain enough decomposed material for XRD measurements.

3. Theoretical methodology

Density functional theory (DFT) with the spin-polarized generalized gradient approximation (GGA) embedded in Vienna *ab initio* simulation package (VASP) was employed.[23–26] The plane-wave basis based projector augmented-wave pseudopotentials were used in the calculation. The valence-electron configurations used in the pseudopotentials are as follows: $4s^24p^64d^15s^2$ for Y, $5s^25p^64f^16s^2$ for Sm, $5d^{10}6s^26p^3$ for Bi, $3p^63d^54s^2$ for Mn, $3d^64s^2$ for Fe, and $2s^22p^4$ for O. To achieve a better description of the systems' total energy and electronic structures, GGA + U method[23,24] and hybrid DFT with Heyd–Scuseria–Ernzerhof approach (HSE06)[27] were applied. All structures in our calculations were relaxed until a force convergence criterion of 0.001 eV nm^{-1} was fulfilled. High 450 eV energy cut-off and a Monkhorst–pack *k*-space sampling mesh with a density of 0.003

nm^{-1} (GGA + U) or 0.01 nm^{-1} (HSE06) for each direction was used to assure an accurate total energy for all the simulated systems. Furthermore, to determine the most likely magnetic state, the structures were relaxed with consideration of all possible spin states. The mullite structure was found to be most stable in a high-spin ferromagnetic state after relaxation. All results shown below are performed in this spin state.

Formation enthalpy calculated by the GGA or GGA + U method still includes significant errors.[28] Therefore, we used corrections on the total energies to improve the accuracy of the ternary compounds' formation enthalpies. Eqn (1) has been used to make the corrections in our calculations.

$$\Delta H_{\mathrm{RMO}} = E_{\mathrm{RMO}}^{\mathrm{GGA+U}} - \left(\sum_{i\in M} n_i \Delta E_i + \sum_{i\in \zeta} n_i E_i\right) \quad (1)$$

where $E_{\mathrm{RMO}}^{\mathrm{GGA+U}}$ is the DFT calculated total energy from GGA + U method, n_i is the number of atom species i in the structure, ζ denotes to all of elements in the calculated compound, M represents the transition metal elements of the U value, and E_i contributes to the pure element energy per atom calculated by GGA method, *i.e.* the metallic form of Bi, Sm, Y, Mn, Fe or oxygen molecule, O_2. Energy adjustment ΔE_i was introduced to correct for the inconsistency between the GGA and GGA + U methods following the procedure proposed by Jain *et al.*[26] To maintain the self-consistency within the simulation, energy adjustments (ΔE_i) and effective interaction parameters ($U_{\mathrm{eff}} = U - J$) were calculated (Table S1, ESI†). The formation enthalpy calculated through this method is at 0 K. Here, configuration differences brought about from zero-point effects are not considered, making this calculation an approximation. However, such contributions have been considered negligible in previous studies.[29,30] To predict the thermal stability of the $R_2(Mn_{1-x}Fe_x)_4O_{10-\delta}$ compounds, we calculated the temperature of the decomposition as detailed in our previous work.[20]

4. Results and discussion

4.1. Mullite-type phase formation with Fe substitution

4.1.1. R = Y, Sm. We first present experimental results of Y and Sm compounds made with three different transition metal compositions: 100% Mn, equal Fe and Mn (50% Fe/50% Mn), and 100% Fe. The multi-phase Rietveld refinement was carried out to determine the phase purity. For the 100% Mn compounds, the crystalline reflections of both R = Y (Fig. 1a, black) and Sm (Fig. 1b, black) corresponds to mullite phase (O10), indicating the formation of $Y_2Mn_4O_{10}$ and $Sm_2Mn_4O_{10}$ with an orthorhombic unit cell, respectively.[20] Both samples are phase-pure with no additional reflections in the XRD patterns.[20] With equal molar concentrations of Fe and Mn in the reactants, the XRD pattern of R = Y sample (Fig. 1a, red) shows the characteristic (121) and (211) reflections (purple inverted triangles) of the mullite-type phase. However, there are additional reflections (green dumbbell) indicating the presence of impure phases in the sample. The phase composition obtained from the Rietveld refinement (Fig. S2a & Table S2, ESI†) indicates that the sample consists of 55% O10 mullite-type phase[14]

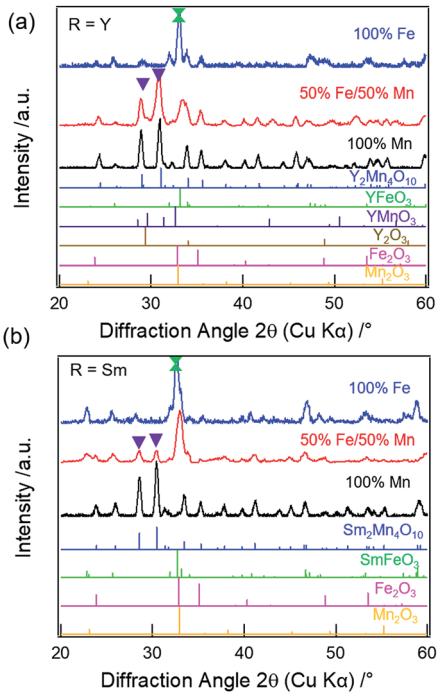

Fig. 1 XRD patterns of (a) R = Y and (b) R = Sm for 100% Mn (black), 50% Fe/50% Mn (red), and 100% Fe (blue). Purple inverted triangles represent the two most intense reflections (121) and (211) of the mullite-type phase and green dumbbell represents the secondary phases.

while the weak reflections correspond to the presence of $YFeO_3$ [31] (21%), Mn_2O_3 (16%), and $YMnO_3$ [32] (7%) impure phases, respectively. For R = Sm, the XRD pattern (Fig. 1b, red) does show weak reflections corresponding to the mullite-type phase (purple inverted triangles), however, the phase purity is only 18%. The primary phases are found to be $SmFeO_3$ (47%) and Mn_2O_3 (35%), respectively (Fig. S2c & Table S2, ESI†). Munoz *et al.* reported the presence of perovskite impurity phase in their $Y_2Mn_2Fe_2O_{10}$ compound, but found that the mullite phase purity can be increased by annealing at 1173 K for 12 h under high oxygen pressure of 200 bar.[14] Thus, one possibility for the presence of the non-mullite-type phases in our samples is the low oxygen partial pressure in the annealing atmosphere. However, as previously reported, complete elimination of the non-mullite-type phase in $R_2Mn_2Fe_2O_{10}$ compounds is not possible for R = Y, Sm, Er, Yb, and Tb, even when the thermal treatments are carried out at high oxygen pressure or when synthesized under mechanical milling.[13–17] The lattice parameters obtained from the refinements for the mullite-type phase are listed in Table S3 (ESI†).

On full replacement of Mn with Fe (100% Fe), XRD patterns of both Y (Fig. 1a, blue) and Sm (Fig. 1b, blue) compounds show no reflections corresponding to mullite phase. The perovskite ($YFeO_3$ (57%) or $SmFeO_3$ (72%)) is found to be the primary phase, along with Y_2O_3 or Sm_2O_3, respectively, and Fe_2O_3 secondary phases. The refined patterns for Y (Fig. S2b†) and Sm (Fig. S2d†) are shown in the ESI.† Thus, mullite-type phase formation is found to be unfavorable when R = Y or Sm at higher Fe concentration.

4.1.2. R = Bi. Fig. 2a shows the XRD patterns of Bi compounds for 100% Mn, 50% Fe/50% Mn, and 100% Fe. The XRD pattern of $Bi_2Mn_4O_{10}$ (Fig. 2a, black) presents no additional reflections indicating 100% pure mullite-type (O10) phase with an orthorhombic unit cell.[20] For 50% substitution of Mn with Fe, the preliminary XRD pattern of $Bi_2Mn_2Fe_2O_{10-\delta}$ (Fig. 2a, red) shows reflections corresponding to mullite-type phase. However, the (210), (201), (002), and (202) reflections exhibit significant broadening compared to the 100% Mn and 100% Fe samples. The XRD results are consistent with the existence of two phases, as Rietveld refinements (Fig. 2b) indicates the presence of $Bi_2Mn_2Fe_2O_{10}$ O10-type (54%),[9] $Bi_2Fe_4O_9$ O9-type (42%),[19] and Mn_2O_3 (4%) (detailed phase compositions are given in Table S2, ESI†). However, since Mn and Fe are very similar, definitive site assignments based on XRD alone are difficult. The XRD pattern (Fig. 2a, blue) of 100% Fe corresponds to $Bi_2Fe_4O_9$ O9 mullite-type compound that can be indexed to the orthorhombic unit cell.[19] The mullite phase purity from the refinement (Fig. S3, ESI†) is found to be 95% along with minor impurity phases of Bi_2O_3 [33] (4%) and $BiFeO_3$ [34] (1%). Thus, a sub-group transition from O10- to O9-type structure is observed for R = Bi when Fe concentration increases from 50% to 100% unlike R = Y or Sm.

The refined lattice parameters for the mullite-type compounds are listed in Table S3 (ESI†). The unit cell volume as a function of Fe concentration for R = Y (blue solid circles), Sm (red solid squares), and Bi (black solid triangles) compounds are depicted in Fig. 3. In general, the unit cell

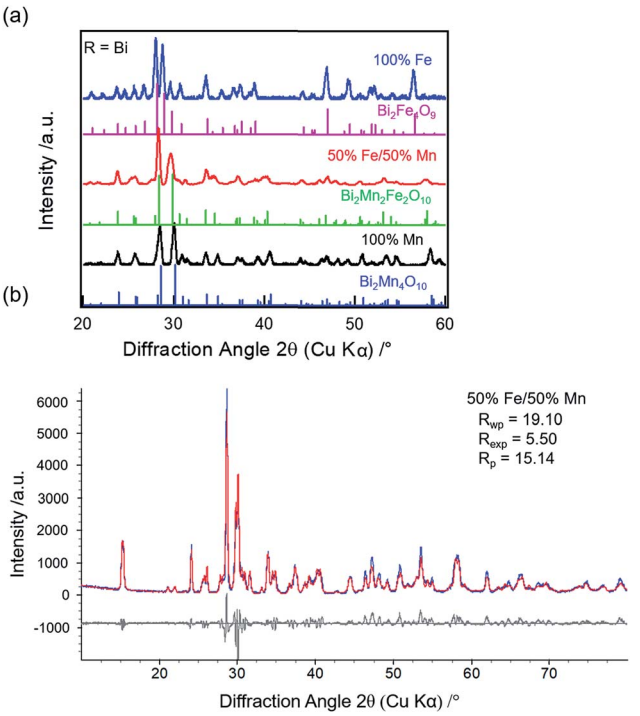

Fig. 2 (a) XRD patterns of R = Bi for 100% Mn (black), 50% Fe/50% Mn (red), and 100% Fe (blue), respectively. Respective reference diffraction data are shown. (b) Experimental (blue), calculated (red), and difference (grey) patterns for Bi compound with 50% Fe/50% Mn in the reactants.

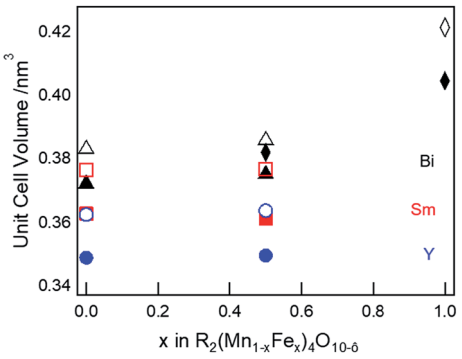

Fig. 3 Experimental (solid symbols) and simulated (open symbols) unit cell volume as a function of Fe in $R_2(Mn_{1-x}Fe_x)_4O_{10-\delta}$ for R = Y (blue circles), Sm (red squares), and Bi (black triangles) O10-type and $Bi_2Fe_4O_9$ (black diamonds) O9-type structures, respectively.

volume systematically decreases with the substitution of a smaller R ions (Y^{3+} < Sm^{3+} < Bi^{3+}) in the O10-type phase, consistent with Vegard's law. Up to 50% Fe in the mullite-type structure, only a small change in the unit cell volume is observed. This observation is consistent with that Fe primarily substitutes for Mn^{3+} in the square pyramidal (4h) sites and given similar ionic radii of Fe^{3+} (0.058 nm) and Mn^{3+} (0.058 nm),[35] cell dimensions do not change significantly upon full substitution in these sites. As Fe concentration exceeds 50% and all Mn^{3+} have been replaced, Fe must substitute on the octahedral (4f) sites. We then observed a significant increase in unit cell volume for $Bi_2Fe_4O_9$ (~9%, black solid diamond), which is attributed to the replacement of smaller Mn^{4+} (0.053 nm)[35] by larger Fe^{3+} ions (0.065 nm)[35] in the octahedral sites. These results show a distinct R-site dependent phase behaviour of mullite-type oxides: only Bi is found to form a stable mullite-type structure at all Mn–Fe compositions. In order to understand this unique behaviour of Bi compared to Y or Sm, we study formation enthalpy and electronic structure using DFT (see Section 4.4 below). Since neither Y nor Sm could form stable Fe substituted mullite-type structures, we carried out the XPS and decomposition studies focusing on Bi O10 and O9-type compounds.

4.2. XPS of $Bi_2(Mn_{1-x}Fe_x)_4O_{10-\delta}$ compounds

XPS studies were carried out on $Bi_2Mn_4O_{10}$, $Bi_2Mn_2Fe_2O_{10-\delta}$, and $Bi_2Fe_4O_9$ stable structures to probe whether there are changes in the oxidation states of Mn and Fe. The measured and fitted XPS spectra of Mn 2p and Fe 2p core-levels are shown in Fig. 4. The Mn 2p spectrum of $Bi_2Mn_4O_{10}$ (Fig. 4a, black) can be deconvoluted into two peaks at 641.2 eV and 641.8 eV, corresponding to the binding energies of $2p_{3/2}$ Mn^{3+} (pink dashed line) and Mn^{4+} (blue dashed line), respectively, in good agreement with the literature.[36] On the other hand, the Mn 2p spectrum of $Bi_2Mn_2Fe_2O_{10-\delta}$ (Fig. 4a, red) exhibits only a single peak at 641.9 eV, corresponding to the binding energy of $2p_{3/2}$ Mn^{4+}.[36] No peak corresponding to Mn^{3+} is found, indicating that 4h square pyramidal sites are fully replaced by Fe. The Fe 2p spectra for $Bi_2Mn_2Fe_2O_{10-\delta}$ (Fig. 4b, red) and $Bi_2Fe_4O_9$

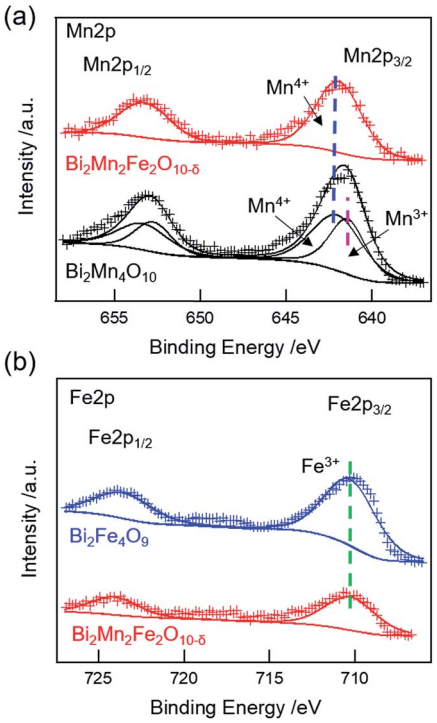

Fig. 4 XPS spectra of (a) Mn 2p core levels in $Bi_2Mn_4O_{10}$ (black) and $Bi_2Mn_2Fe_2O_{10-\delta}$ (red) samples, respectively. (b) Fe 2p core levels in $Bi_2Mn_2Fe_2O_{10-\delta}$ (red) and $Bi_2Fe_4O_9$ (blue) samples, respectively. The pink, blue, and green dashed lines show the binding energies for Mn^{3+}, Mn^{4+}, and Fe^{3+} signals, respectively.

(Fig. 4b, blue) is fitted to a single peak. The binding energy of Fe $2p_{3/2}$ at 710.3 eV (Fig. 4b, green dashed line) corresponds to 3+ oxidation state.[36] No peaks corresponding to Fe^{4+} (712.5 eV)[37] are found in either structure. The XPS results are consistent with Rietveld refinement of the XRD results for this sample, which shows the co-existence of $Bi_2Mn_2Fe_2O_{10}$ and $Bi_2Fe_4O_9$. Mn ions in $Bi_2Mn_2Fe_2O_{10}$ are exclusively in the 4f sites, *i.e.* 4+, and Fe ions occupy the 4h sites, *i.e.* 3+, while Fe in both sites of $Bi_2Fe_4O_9$ have 3+ oxidation state. We further calculated the Fe/Mn and (Mn + Fe)/Bi ratios of the $Bi_2Mn_2Fe_2O_{10-\delta}$ sample following Gesing *et al.* in order to understand which metal is enriched on the surface layers.[38] The surface Fe/Mn ratio is found to be 0.73 ± 0.13, indicating that the surface is enriched with Mn, while (Mn + Fe)/Bi is found to be 1.61 ± 0.11 compared to the formula ratio of 2. These results indicate that the Fe composition is intrinsic to the bulk phase rather than only on the surface. Combined XRD and XPS results show that Fe^{3+} ions preferentially occupy 4h square-pyramidal and Mn^{4+} occupy 4f octahedral sites in $Bi_2Mn_2Fe_2O_{10-\delta}$. While in $Bi_2Fe_4O_9$, Fe^{3+} ions are distributed in tetrahedral and octahedral sites, respectively.

4.3. Thermal stability and decomposition reaction of $Bi_2(Mn_{1-x}Fe_x)_4O_{10-\delta}$

We further carried out TGA-DSC measurements of $Bi_2(Mn_{1-x}Fe_x)_4O_{10-\delta}$ compounds to study their thermal stability. 100% Mn compound, *i.e.* $Bi_2Mn_4O_{10}$, is found to be thermally stable until 1217 K as reported in our previous work.[20] Fig. 5a shows the TGA-DSC data of calcined $Bi_2Mn_2Fe_2O_{10-\delta}$ sample heated from room temperature to 1273 K in air. We observe a clear weight loss in TGA (Fig. 5a, black) and a corresponding endothermic peak in DSC (Fig. 5a, red), which may be attributed to the thermal decomposition of the sample. The temperature associated with the thermal event is 1142 K, determined from the onset of weight loss. In order to establish that the observed weight loss corresponds to thermal decomposition in the sample and to determine the decomposed product(s) using XRD, we mimicked the TGA experiment by heating the calcined $Bi_2Mn_2Fe_2O_{10-\delta}$ sample in a furnace from room temperature to 1173 K in air without dwell time at the final temperature. Note that a different aliquot of the same sample used in the TGA-DSC experiment was used here. The XRD pattern of the sample heated above the decomposition temperature (Fig. 5b, red) shows no diffraction peak corresponding to the mullite-type phase (Fig. 5b, purple inverted triangles) when compared to the XRD pattern of the as-synthesized sample (Fig. 5b, black). On further examining the diffraction pattern (Fig. 5b, red), we find that the mullite-type phase decomposes primarily to $BiFeO_3$ perovskite along with Bi_2O_3, Fe_2O_3, and Mn_2O_3 secondary phases; no reflections corresponding to the $BiMnO_3$ perovskite phase are found. Based on the decomposed products, we propose the decomposition reaction for $Bi_2Mn_2Fe_2O_{10-\delta}$ compound in eqn (2):

$$Bi_2Fe_2Mn_2O_{10-\delta}(> 1142\ \ K) = BiFeO_3 + \frac{1}{2}Bi_2O_3 + \frac{1}{2}Fe_2O_3 + Mn_2O_3 + \frac{(1-\delta)}{2}O_2 \quad (2)$$

Attributing the weight loss in TGA at 1142 K (Fig. 5a, black) to the oxygen loss upon decomposition, we find $\delta = 0.6$. When compared to the decomposition temperature of $Bi_2Mn_4O_{10}$, incorporation of 50% Fe in the mullite-type structure lowers the thermal stability by ~75 K. Moreover, in contrast to $Bi_2Mn_4O_{10}$, where only binary oxides were found upon decomposition,[20] the formation of $BiFeO_3$ perovskite is found in $Bi_2Mn_2Fe_2O_{10-\delta}$ decomposition. Note that this sample exhibits a second thermal event at ~1190 K, which has no associated weight loss. Having two decomposition temperatures are consistent with the sample having two phases: the mixed Fe–Mn O10 phase decomposes at lower temperature and the Fe O9 phase decomposes at higher temperature (see below).

Heating the already calcined $Bi_2Fe_4O_9$ sample from room temperature to 1273 K in the TGA-DSC experiment results in a small weight loss (Fig. 5c, black) along with an endothermic peak (Fig. 5c, red), which may correspond to the thermal decomposition of $Bi_2Fe_4O_9$ phase. The weight loss at this temperature (Fig. 5c, black) is small compared to $Bi_2Mn_2Fe_2O_{10-\delta}$ sample, 0.05% *vs.* 0.8% (Fig. 5a, black). To investigate this transition, we heated the calcined $Bi_2Fe_4O_9$ sample from room temperature to 1273 K in air without dwell time at the final temperature. The XRD pattern (Fig. 5d, red) confirms the thermal decomposition of the $Bi_2Fe_4O_9$ as no characteristic

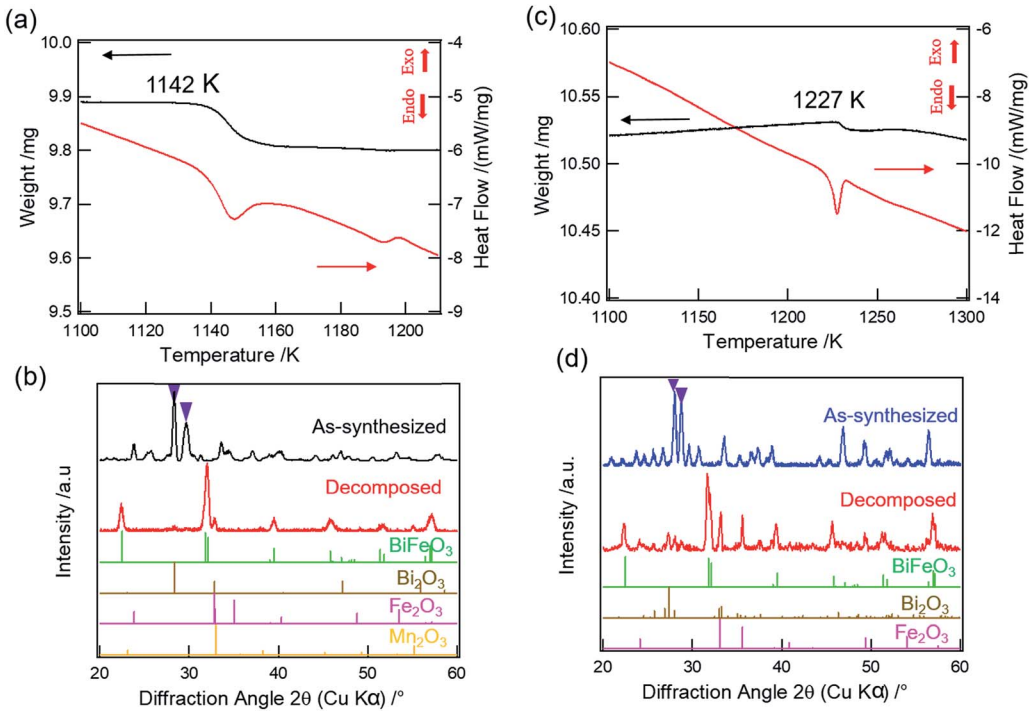

Fig. 5 (a, c) Zoom in view of TGA (black) and DSC (red) curves of $Bi_2Mn_2Fe_2O_{10-\delta}$ and $Bi_2Fe_4O_9$, respectively. (b) XRD patterns of as-synthesized $Bi_2Mn_2Fe_2O_{10-\delta}$ (black) and decomposed (red) samples, respectively. (d) XRD patterns of as-synthesized $Bi_2Fe_4O_9$ (blue) and decomposed (red) samples, respectively. Respective reference diffraction data are shown. Purple inverted triangles represent the two most intense reflections (121) and (211) of mullite-type phase.

reflections of mullite-type phase (Fig. 5d, purple inverted triangles) are found when compared to the diffraction pattern of the as-synthesized sample (Fig. 5d, blue). The decomposition results primarily in the formation of the $BiFeO_3$ perovskite phase along with Bi_2O_3 and Fe_2O_3 secondary phases. We therefore propose the decomposition reaction for $Bi_2Fe_4O_9$ as given in eqn (3):

$$Bi_2Fe_4O_9\ (>1227\ K) = BiFeO_3 + \frac{1}{2}Bi_2O_3 + \frac{3}{2}Fe_2O_3 \quad (3)$$

As eqn (3) shows, this decomposition reaction does not release oxygen, consistent with very small weight loss observed in TGA. One possibility is that the decomposition may be caused by the vaporization of Bi_2O_3 which is reported to occur above 1100 K, thus resulting in a small weight loss during decomposition.[39,40] The second possibility is the creation of oxygen vacancies in the decomposed Bi_2O_3 and Fe_2O_3 as shown in the DFT calculations (Section 4.4.3); the small amount of oxygen loss (0.03 oxygen atom) during decomposition can be attributed to the creation of oxygen vacancies in the decomposition products. These results show that $Bi_2Mn_4O_{10}$ and $B_2iFe_4O_9$ are thermally more stable than $Bi_2Mn_2Fe_2O_{10-\delta}$. To explain the experimentally observed differences, we present DFT calculation results below.

4.4. DFT calculations

4.4.1. Formation enthalpy. To elucidate the role of R-site elements on mullite-type phase formation, we used DFT modelling to calculate the formation enthalpy of compounds with varying Fe/Mn ratios. Ground state structures are obtained by examining various Fe substitution configurations in a single unit cell. In our simulation, less negative formation enthalpy indicates that the structure is energetically less favourable. Therefore, we could identify the most stable structure by examining the structure with the most negative formation enthalpy. The change in formation enthalpy with respect to $R_2Mn_4O_{10}$ (ΔH) for R = Y (Fig. 6, blue open circles), Sm (Fig. 6, red open squares), and Bi (Fig. 6, black open triangles) O10-type compounds is found to monotonically increase with Fe content in the structure. For low Fe concentration ($x < 0.6$), ΔH is small ($\sim$0.1 eV at $x = 0.5$) indicating stable mullite-type structures can be formed independent of R-site elements. This is due to Fe substitution into the 4h pyramidal sites being more stable than the substitution of Fe into the 4f octahedral sites. Although the simulation indicates that stable mullite-type structures can be formed for R = Y, Sm, or Bi with 50% Fe and 50% Mn in the reactants, experimentally pure mullite-type phases could only be formed for Bi (Fig. 2a, red), not for Y (Fig. 1a, red) and Sm (Fig. 1b, red). As the Fe concentration increases past $x = 0.6$, a stronger dependence on the R-site element is seen, along with a large change in the formation enthalpy indicating that the O10-type structure becomes less stable. Since all 4h sites are occupied, a further increase in the Fe concentration forces the remaining Fe into the 4f octahedral sites. Consequently, the structure becomes unstable as Fe in the octahedral site of the O10-type structure is 4+ with a large Jahn–Teller distortion. Thus, a sub-group transition occurs as Fe increases to 100%

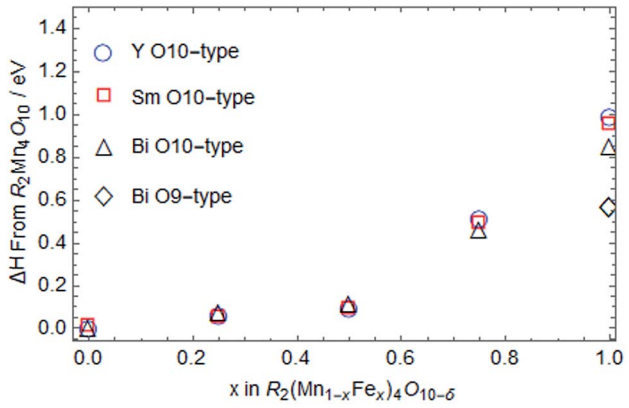

Fig. 6 Calculated change in formation enthalpy for $R_2(Mn_{1-x}Fe_x)_4O_{10-\delta}$ O10-type compounds for R = Y (blue open circles), Sm (red open squares), and Bi (black open triangles) with increasing amount of Fe in the structure. $Bi_2Fe_4O_9$ ($x = 1$) O9-type phase is also stable and shown as black open diamond.

(Fig. 6, black open diamond). Consequently, the octahedral site's charge state is reduced, hence allowing Fe^{3+} substitution in the chain, consistent with XPS result (Fig. 4b, blue) where only Fe^{3+} was found. Additionally, the reduction in O content leads to changing from MO_5 square pyramidal (Fig. S1b, ESI†) to MO_4 tetrahedral units (Fig. S1c, ESI†). We further summarize the obtained ground state structure and lattice parameter for (Y, Sm, Bi)$_2(Mn_{1-x}Fe_x)_4O_{10-\delta}$ O10-type and $Bi_2Fe_4O_9$ O9-type compounds in Table S3 (ESI†). The calculated lattice parameters, hence unit cell volumes (Fig. 3, open symbols), are found to increase with an increase in Fe incorporation in the mullite-type structure and are in good agreement with the experimental values.

4.4.2. Electronic structure. We calculated the electronic structures to elucidate why (1) $Bi_2Fe_4O_9$ (O9) is stable while $Bi_2Fe_4O_{10}$ (O10) is not, and (2) why mullite-type structure forms over the entire Mn–Fe compositions only when R = Bi.

To answer the first question, we show the Fe and Mn density of states (DOS) in both 4f octahedral and 4h tetrahedral sites for O9 and O10-type structure in Fig. S4 & S5 (ESI†). We found that Fe^{4+} in the 4f octahedral sites of O10-type structure causes large Jahn–Teller distortion, which results in mid band-gap empty states, thus violating Hund's rule through the exchange interaction. This does not occur in the O9-type structure. Therefore, the $Bi_2Fe_4O_{10}$ O10-type structure becomes unstable.

Although Y, Sm, and Bi are all in 3+ oxidation states, mullite-type structure is found only for R = Bi compounds at high Fe concentrations, indicating Bi mullite-type compounds have lower structural destabilization with increasing Fe substitution compared to other R-site compounds. In order to understand this phenomenon, we considered the R-site contribution to the electronic structure. In Fig. 7a & b, the projected-DOS of Bi in stable O10 and O9-type structures, respectively are illustrated. Significant sp orbital hybridization for Bi is observed in O9-type (Fig. 7b) near the Fermi level. Bi–O sp-antibonding states near the Fermi surface hybridizing with Bi p-electrons help stabilize the crystal structure.[41] Such hybridization is only limited to near the Fermi level in the O10-type structures (Fig. 7a) due to the high oxidation state of Bi in the local crystal fields. In contrast, due to the shift of p and s orbitals towards the Fermi level in the DOS, more p-electron contribution is found in the hybridization below the Fermi surface in the O9-type structure (Fig. 7b). This is shown by the almost identical and overlapping s and p orbitals right below the Fermi level. As shown in Fig. 7c, we find that excessive p-electrons promote sp hybridization, which further stabilize Bi orbital energy. The outcome of the enhanced sp hybridization is shown to be the directional polarization of Bi electrons (Fig. 7d). In this case, a repulsive force between the Bi atoms could be introduced, thus maintaining the structure's framework along the *ab*-plane. The polarization resulted in elongation of the crystal lattice in *a*–*b* direction (Bi–Bi length was prolonged from 0.37 nm to 0.42 nm) further facilitate Fe forming MO_4 tetrahedral polyhedral without any distortion.

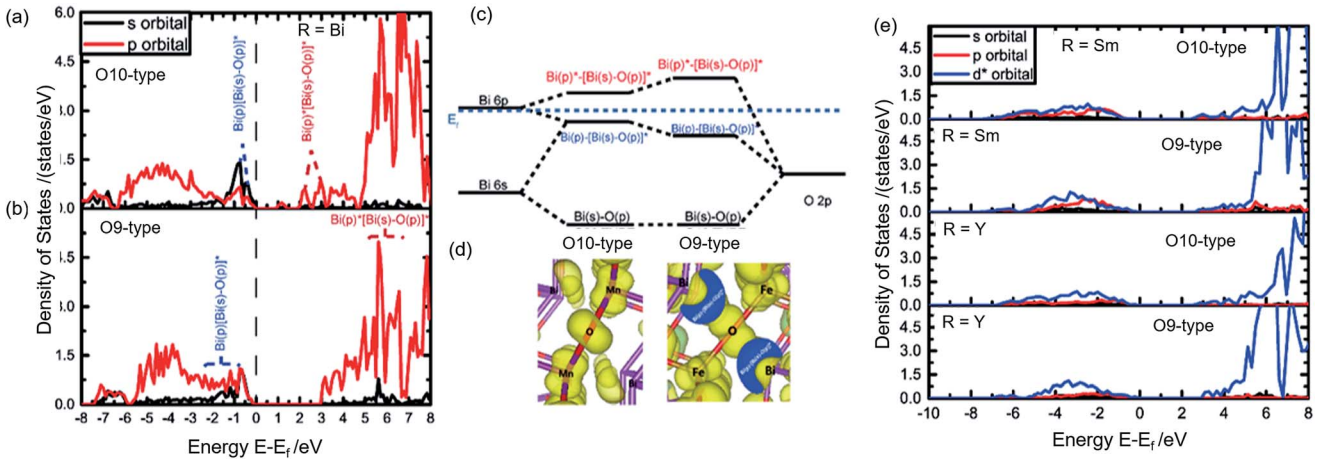

Fig. 7 Projected-DOS of Bi in (a) $Bi_2Mn_4O_{10}$ (O10) and (b) $Bi_2Fe_4O_9$ (O9). (c) Scheme of Bi–O bonding orbital energy levels in O10 (left) and O9-type (right) structures. (d) Projected charge distribution of sp-hybridization in O10 and O9-type structures (the two-charge distribution are drawn in the same isosurface for detailed comparison). (e) Projected-DOS for R = Y and Sm in $R_2Mn_4O_{10}$ (as a representative of O10-type structures) and $R_2Fe_4O_9$ (as a representative of O9-type structures). Each figure is labelled according to the species and its corresponding structures.

Unlike Bi, electronic structures of Sm and Y compounds (Fig. 7e) show that the extra charge from the O10 to O9-type transition would fill up 4d orbital in Y and the 4f orbital in Sm. These orbitals are compact and do not hybridize, thus failing to form the necessary directional polarization that is required to maintain a stable structure. Hence, Y and Sm cannot form stable O9-type phase while Bi can. Since O10-type is unstable due to the Jahn–Teller distortion of Fe^{4+} at high Fe content and no sp hybridization exists to stabilize the O9-type structure, compounds with R = Y or rare earth elements do not form mullite-type structures at these temperatures.

4.4.3. Thermal stability. The effect of R-site elements on the thermal stability of mullite-type compounds is further examined by calculating the decomposition temperature as a function of Fe. For R = Y (Fig. 8a, blue open circles), Sm (Fig. 8b, red open squares), and Bi (Fig. 8c, black open triangles) O10-type show similar trend where the decomposition temperature decreases with increase in Fe concentration. For example, $Bi_2Mn_2Fe_2O_{10-\delta}$ has lower decomposition temperature compared to $Bi_2Mn_4O_{10}$ (1150 K *vs.* 1213 K) in agreement with experimental result (1142 K *vs.* 1217 K) as shown in Fig. 8c (black solid triangle). However, simulations reveal that different R-site elements yield different decomposition temperature for the same amount of Fe in the structure. For example, at $x = 0.5$, the stable temperature limit for Y and Sm is predicted to be 1358 K (Fig. 8a, blue open circle) and 1346 K (Fig. 8b, red open square), respectively. Experimentally, the compound with R = Y and equal Fe and Mn in the reactants (although not pure mullite-type phase) is found to be thermally stable up to 1358 K and decomposes primarily to $YFeO_3$ along with Y_2O_3, Fe_2O_3, and Mn_3O_4 secondary phases (Fig. S6a & b, ESI†). On the other hand, Bi has a lower thermal stability of 1150 K (Fig. 8c, black open triangle) when compared to Y and Sm for the same amount of Fe (50%), which is consistent with the experimental result (Fig. 8c, black solid triangle).

As we further increase the Fe concentration ($x \geq 0.6$), the decomposition temperature of O10-type structure falls below the calcination temperature (Fig. 8a–c, pink dashed line). Consequently, the O10-type structure cannot be formed for all R-site elements studied in this report. Thus, combined experimental and theoretical results show that the thermal stability of O10-type structures decreases with increasing Fe concentration. With respect to the calcination temperature used in this report (1073 K), the substitution limit for Fe in R = Y and Sm O10-type compounds are predicted to be $x \leq 0.6$. However, simulation predicts O10 structures, if formed, to have higher thermal stability for Y and Sm than Bi compound.

Considering the thermal stability of O9-type structures, Y (Fig. 8a, blue open dumbbells) and Sm (Fig. 8b, red open pentagons) are found to be thermodynamically unstable for all Fe/Mn ratios. On the other hand, Bi O9-type is calculated to have a distinct decomposition temperature in Fe rich structures

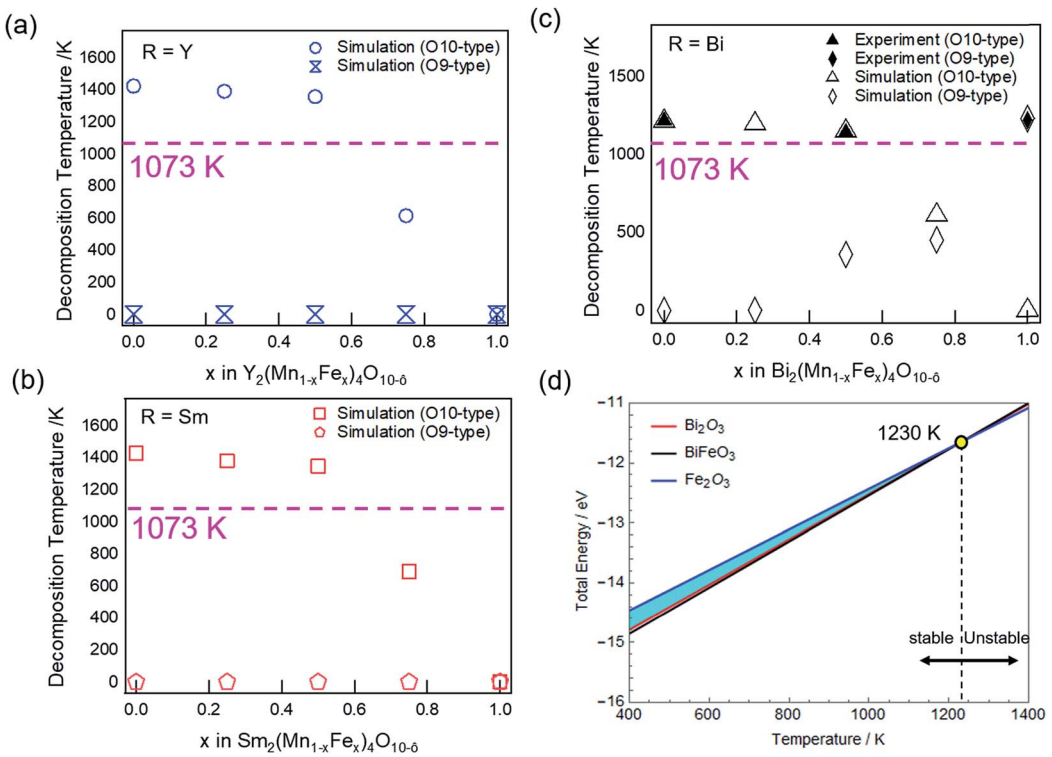

Fig. 8 Simulated decomposition temperature as a function of Fe for (a) R = Y O10 (blue open circles) and O9-type (blue open dumbbells). (b) R = Sm O10 (red open squares) and O9-type (red open pentagons). (c) R = Bi O10 (black open triangles) and O9-type (black open diamonds); experimental O10 (black solid triangles) and O9-type (black solid diamond) are shown. Pink dashed line indicates the calcination temperature employed. (d) Thermal stability diagram of $Bi_2Fe_4O_9$ showing the stable region and decomposition temperature. Yellow solid circle represents the decomposing products corresponding to $BiFeO_3$ (black), Bi_2O_3 (red), and Fe_2O_3 (blue) at 1230 K.

(Fig. 8c, black open diamonds). The decomposition temperature is found to increase with Fe concentration, but for $x < 1$, the decomposition temperature is below the calcination temperature (Fig. 8c, pink line), hence unable to form O9-type structure. The decomposition temperature for $Bi_2Fe_4O_9$ (at $x = 1$) is calculated to be 1230 K, which is higher than $Bi_2Mn_2Fe_2O_{10-\delta}$ (1150 K) and in good agreement with the experimental result.

Fig. 8d shows the change in total energy as a function of temperature for $Bi_2Fe_4O_9$. The solid lines define the boundaries where precipitation of the compound begins under the simulated $Bi_2Fe_4O_9$ calcination conditions. The blue shaded region (Fig. 8d) represents the phase space where $Bi_2Fe_4O_9$ is stable in the system. The upper limit of the stable region is confined by Fe_2O_3 (Fig. 8d, blue line) while the lower limit is governed by Bi_2O_3 (Fig. 8d, red line) and $BiFeO_3$ (Fig. 8d, black line) phases. The temperature at which $BiFeO_3$, Bi_2O_3, and Fe_2O_3 converge defines the limit of the $Bi_2Fe_4O_9$ stable region, predicted to be 1230 K (Fig. 8d, yellow circle), in agreement with the experimental value of 1227 K. Further increasing the temperature will result in decomposition to $BiFeO_3$, Bi_2O_3, and Fe_2O_3 phases, as in the experimental decomposition products (Fig. 5d, red).

Since the formation enthalpy of $Bi_2Fe_4O_9$ is ~0.6 eV higher than that of $Bi_2Mn_4O_{10}$ (Fig. 6), one would expect the decomposition temperature of $Bi_2Fe_4O_9$ to be much lower than that of $Bi_2Mn_4O_{10}$. Examining the stereochemical activity of Bi lone electron pair also lead to the same conclusion.[42] In contrast, experimentally we observed the reverse, 1227 K for $Bi_2Fe_4O_9$ *vs.* 1217 K for $Bi_2Mn_4O_{10}$. The reason is that the decomposition products of $Bi_2Fe_4O_9$ are also less stable than those for $Bi_2Mn_4O_{10}$, with 0.8 eV per formula unit higher energy. In addition, examining the stability of oxygen vacancies in Fe_2O_3, Bi_2O_3, and $BiFeO_3$, we find that these oxygen deficient phases are more stable than their stoichiometric oxides. More oxygen vacancies are expected in Bi_2O_3 because its formation enthalpy only increases by 0.58 eV per unit cell for one oxygen vacancy, *vs.* 2.78 eV and 2.97 eV increase in the formation enthalpy for one oxygen vacancy in Fe_2O_3 and $BiFeO_3$, respectively. Oxygen vacancy formation in the decomposition products could explain the observed non-zero weight loss during the decomposition of $Bi_2Fe_4O_9$ (Fig. 5c, black), although we cannot rule out the vaporization of Bi_2O_3. In Fig. 8d, both Fe_2O_3 and Bi_2O_3 were plotted with small vacancy amounts as required to cause decomposition. After taking into account everything discussed above, we calculated $Bi_2Fe_4O_9$ to have a higher decomposition temperature than $Bi_2Mn_4O_{10}$ (1230 K *vs.* 1213 K), as borne out by experiments.

5. Conclusions

In summary, we investigated R-site dependent phase formation and thermal stability of $R_2(Mn_{1-x}Fe_x)_4O_{10-\delta}$ compounds. For the Mn compounds, Y, Sm, and Bi analogues are found to form pure O10 mullite-type phase with an orthorhombic unit cell. However, with 50% Fe and 50% Mn in the reactants, only 55% and 18% of the products when R = Y and Sm consists of (Y, Sm)$_2Mn_2Fe_2O_{10-\delta}$ mullite-type phase, respectively, whereas Bi forms a mixed phase of O10-($Bi_2Mn_2Fe_2O_{10-\delta}$, 54%) and O9-($Bi_2Fe_4O_9$, 42%) type structures. Furthermore, when the reactants contain 100% Fe, the mullite-type structure completely destabilizes for Y and Sm, but a sub-group transition to $Bi_2Fe_4O_9$ (O9) phase is found for R = Bi. From XPS, we determine that the Mn and Fe exists in 4+ and 3+ oxidation states in $Bi_2Mn_2Fe_2O_{10-\delta}$, respectively, indicating Mn^{4+} and Fe^{3+} are ordered in 4f octahedra and 4h square pyramids. While in $Bi_2Fe_4O_9$, only Fe^{3+} is found, consistent with Fe^{4+} destabilizing O10-type structure. The thermal stability shows a decreasing decomposition temperature with increasing Fe concentration in O10-type structures (1142 K for $Bi_2Mn_2Fe_2O_{10-\delta}$ *vs.* 1217 K for $Bi_2Mn_4O_{10}$) while $Bi_2Fe_4O_9$ is found to decompose at the highest temperature (1227 K). Our DFT simulation confirms distinctly different phase behaviors among R = Y, Sm, and Bi compounds as observed experimentally and predicts Fe substitution limits for R = Y and Sm for the formation of mullite-type structure to be $x < 0.6$. The R-site dependent phase behaviors arise from the combination of unstable Fe^{4+} Jahn–Teller distortion in MO_6 octahedra and orbital hybridization of R-site element. While Fe inevitably destabilizes the O10-type structure with increasing Fe concentration, we find that the directional sp orbital hybridization in Bi effectively stabilizes the O9 mullite-type structure. Y and rare earth elements do not have sp hybridization, and hence are unable to form O9-type structure. Our work provides a fundamental understanding for the unique phase behavior of Bi Mn–Fe mullite-type compounds previously reported in the literature without explanation.

Conflicts of interest

There are no conflicts to declare.

Acknowledgements

We thank J. M. Kweun, M. Cho, Y. Y. Kim for helpful discussions at the initial stage of this research. This work was funded in part by a grant (AT-1843) from the Welch Foundation and a funding from International Energy Joint R & D Program (No. 20168510011350) of the Korea Institute of Energy Technology Evaluation and Planning (KETEP) grant funded by the Ministry of Knowledge Economy. J. Y. C acknowledges NSF-DMR #1700030 for partial support. J. W. P. H acknowledges the Texas Instruments Distinguished Chair in Nanoelectronics.

Notes and references

1 L. M. Volkova and D. V. Marinin, *J. Phys.: Condens. Matter*, 2009, **21**(015903), 1–14.
2 J. A. Alonso, M. T. Casais, M. J. Martínez-Lope, J. L. Martínez and M. T. Fernández-Díaz, *J. Phys.: Condens. Matter*, 1997, **9**, 8515–8526.
3 I. Abrahams, A. J. Bush, G. E. Hawkes and T. Nunes, *J. Solid State Chem.*, 1999, **147**, 631–636.
4 Q. Ruan and W. Zhang, *J. Phys. Chem. C*, 2009, **113**, 4168–4173.

5 W. Wang, G. McCool, N. Kapur, G. Yuan, B. Shan, M. Nguyen, U. M. Graham, B. H. Davis, G. Jacobs, K. Cho and X. Hao, *Science*, 2012, **337**, 832–835.
6 Z. Feng, J. Wang, X. Liu, Y. Wen, R. Chen, H. Yin, M. Shen and B. Shan, *Catal. Sci. Technol.*, 2016, **6**, 5580–5589.
7 S. Thampy, Y. Zheng, S. Dillon, C. Liu, Y. Jangjou, Y. J. Lee, W. S. Epling, K. Xiong, Y. J. Chabal, K. Cho and J. W. P. Hsu, *Catal. Today*, 2017, DOI: 10.1016/j.cattod.2017.05.008.
8 R. X. Fischer and H. Schneider, Mullite, in *The mullite-type family of crystal structures*, ed. H. Schneider and S. Komarneni, John Wiley & Sons, 2006, pp. 16–18.
9 N. Niizeki and M. Wachi, *Z. Kristallogr.*, 1968, **127**, 173–187.
10 M. Burianek, T. F. Krenzel, M. Schmittner, J. Schreuer, R. X. Fischer, M. Muhlberg, G. Nenert, H. Schneider and T. M. Gesing, *Int. J. Mater. Res.*, 2012, **103**, 449–455.
11 M. M. Murshed, G. Nenert, M. Burianek, L. Robben, M. Muhlberg, H. Schneider, R. X. Fischer and T. M. Gesing, *J. Solid State Chem.*, 2013, **197**, 370–378.
12 H. Schneider, R. X. Fischer, T. M. Gesing, J. Schreuer and M. Muhlberg, *Int. J. Mater. Res.*, 2012, **103**, 422–429.
13 J. A. Alonso, M. J. Martínez-Lope and J. L. Martínez, *Phys. Rev. B*, 2005, **72**(184402), 1–8.
14 A. Munoz, J. A. Alonso, M. J. Martínez-Lope and J. L. Martínez, *Chem. Mater.*, 2004, **16**, 4087–4094.
15 K. S. Kumar, N. Aparnadevi, A. Muthukumaran and C. Venkateswaran, *Trans. Indian Inst. Met.*, 2015, **68**, 693–698.
16 M. J. Martínez-Lope, M. Retuerto, J. A. Alonso, M. García-Hernández, K. Krezhov, I. Spirov, T. Ruskov and M. T. Fernández-Díaz, *Solid State Commun.*, 2009, **149**, 540–545.
17 M. Retuerto, M. J. Martínez-Lope, A. Muñoz, T. Ruskov, I. Spirov, K. Krezhov, M. T. Fernández-Díaz, M. García-Hernández and J. A. Alonso, *Solid State Commun.*, 2010, **150**, 1831–1836.
18 K. S. Kumar and C. Venkateswaran, *J. Phys. D: Appl. Phys.*, 2011, **44**(325001), 1–6.
19 Z. R. Kann, J. T. Auletta, E. W. Hearn, S. U. Weber, K. D. Becker, H. Schneider and M. W. Lufaso, *J. Solid State Chem.*, 2012, **185**, 62–71.
20 C. Li, S. Thampy, Y. Zheng, M. Kweun, Y. Ren, J. Y. Chan, H. Kim, M. Cho, Y. Y. Kim, J. W. P. Hsu and K. Cho, *J. Phys.: Condens. Matter*, 2016, **28**(125602), 1–10.
21 S. Thampy, V. Ibarra, Y. Lee, G. McCool, K. Cho and J. W. P. Hsu, *Appl. Surf. Sci.*, 2016, **385**, 490–497.
22 M. H. Mendenhall, A. Henins, L. T. Hudson, C. I. Szabo, D. Windover and J. P. Cline, *J. Phys. B: At., Mol. Opt. Phys.*, 2017, **50**(115004), 1–18.
23 G. Kresse and J. Furthmuller, *Comput. Mater. Sci.*, 1996, **6**, 15–50.
24 D. C. Langreth and M. J. Mehl, *Phys. Rev. B*, 1983, **28**, 1809–1834.
25 S. L. Dudarev, G. A. Botton, S. Y. Savrasov, C. J. Humphreys and A. P. Sutton, *Phys. Rev. B*, 1998, **57**, 1505–1509.
26 A. Jain, G. Hautier, S. P. Ong, C. J. Moore, C. C. Fischer, K. A. Persson and G. Ceder, *Phys. Rev. B*, 2011, **84**(045115), 1–10.
27 O. A. Vydrov and G. E. Scuseria, *J. Chem. Phys.*, 2006, **125**(234109), 1–9.
28 G. Bergerhoff, R. Hundt, R. Sievers and I. D. Brown, *J. Chem. Inf. Model.*, 1983, **23**(2), 66–69.
29 L. Wang, T. Maxisch and G. Ceder, *Chem. Mater.*, 2007, **19**, 543–552.
30 S. Lany, *Phys. Rev. B*, 2008, **78**(245207), 1–8.
31 P. Coppens and M. Eibschutz, *Acta Crystallogr.*, 1965, **19**, 524–531.
32 K. Lukaszewicz and K. Kalicinska, *Ferroelectrics*, 1974, **7**, 81–82.
33 E. M. Levin and R. S. Roth, *J. Res. Natl. Bur. Stand., Sect. A*, 1963, **68**, 189–195.
34 S. A. Fedulov, Y. N. Venevtsev, G. S. Zhdanov, E. G. Smazhevskaya and I. S. Rez, *Kristallografiya*, 1962, **7**, 77.
35 R. D. Shannon, *Acta Crystallogr., Sect. A: Found. Crystallogr.*, 1976, **32**, 751–769.
36 M. C. Biesinger, B. P. Payne, A. P. Grosvenor, L. W. M. Lau, A. R. Gerson and R. C. Smart, *Appl. Surf. Sci.*, 2011, **257**, 2717–2730.
37 M. Ghaffari, M. Shannon, H. Hui, O. Tan and A. Irannejad, *Surf. Sci.*, 2012, **606**, 670–677.
38 T. M. Gesing, M. Schowalter, C. Weidenthaler, M. M. Murshed, G. Nenert, C. B. Mendive, M. Curti, A. Rosenauer, J.-C. Buhl, H. Schneider and R. X. Fischer, *J. Mater. Chem.*, 2012, **22**, 18814–18823.
39 S.-U. Weber, T. M. Gesing, G. Eckold, R. X. Fischer, F.-J. Litterst and K.-D. Becker, *J. Phys. Chem. Solids*, 2014, **75**, 416–426.
40 A. Maitre, M. Francois and J. C. Gachon, *J. Phase Equilib. Diffus.*, 2004, **25**, 59–67.
41 K. E. Kweon and G. S. Hwang, *Phys. Rev. B*, 2012, **8**(165209), 1–8.
42 M. Curti, T. M. Gesing, M. M. Murshed, T. Bredow and C. B. Mendive, *Z. Kristallogr.*, 2013, **228**, 629–634.